

Recession of an EB-PVD YSZ Coated Turbine Blade by CaSO_4 and Fe, Ti-Rich CMAS-Type Deposits

Wolfgang Braue and Peter Mechnich[†]

German Aerospace Center (DLR), Institute of Materials Research, 51170, Cologne, Germany

An in-service high-pressure turbine blade with a columnar, Y_2O_3 -stabilized ZrO_2 (YSZ) thermal barrier coating (TBC) fabricated by electron-beam physical vapor deposition was investigated to access the TBC hot corrosion mechanisms during turbine operation. The TBC exhibits a through-thickness pore filling with anhydrite-type CaSO_4 . Chemical analysis of the CMAS-type particle deposits reveals relatively low SiO_2 but high CaO contents and substantial amounts of Fe_2O_3 and TiO_2 . The hot corrosion scenario observed at the YSZ column tips involves newly formed CaZrO_3 and the garnet-type phase $\text{Ca}_3(\text{Zr,Mg,Ti})_2(\text{Fe,Al,Si})_3\text{O}_{12}$, also known as the mineral kimzeyite. The phase relationships were confirmed in laboratory experiments. CaSO_4 as well as the particle deposits prove to be effective solvents for YSZ introducing distinct solid-state reactions. The results support the idea of a dual YSZ hot corrosion process. A first stage controlled by a SiO_2 -free Ca-source, most likely primary CaSO_4 produces a thin CaZrO_3 layer. A second, CMAS-type stage providing high concentrations of Fe_2O_3 , TiO_2 , and SiO_2 favors the formation of kimzeyite. The melting temperature of kimzeyite presumably defines a thermal operation limit for YSZ-based TBCs.

I. Introduction

THE state-of-the art material for thermal barrier coatings (TBC) of turbine engine airfoils is tetragonal Y_2O_3 partially stabilized ZrO_2 (YSZ). YSZ TBCs are usually fabricated by electron-beam physical vapor deposition (EB-PVD). EB-PVD produces a characteristic columnar and highly porous microstructure, showing beneficial strain-tolerance and a favorable low thermal conductivity.¹ Ingestion of airborne mineral dust during in-flight operation defines a serious issue for aero-engine performance and service life which has stimulated considerable research effort in industry and academia.^{2–6} Upon heating in the combustor section molten or partially molten mineral particles impinge on hot surfaces. Besides possible reductions in air flow via clogging of turbine cooling air passages⁷ the covering and infiltration of EB-PVD YSZ TBCs of turbine blades by molten inorganic particles is considered a major threat to the lifetime of turbine engines. The spallation of the melt-infiltrated TBC upon thermal cycling has been interpreted as a cold shock effect and is generally recognized as a key failure mechanism of YSZ-based TBCs in the 100 to some 1000 h lifetime range.⁸

Synthetic inorganic materials have been successfully employed in model infiltration experiments to approximate the particle-induced TBC recession.⁹ Most prominent are

compositions equivalent to congruently melting eutectics in the quaternary system $\text{CaO-MgO-Al}_2\text{O}_3\text{-SiO}_2$ (“CMAS”). Above the melting temperature (approx. 1230°C) this model CMAS is able to fully penetrate a 200 μm EB-PVD YSZ TBC in a few hours.

The blades and vanes of the first stage of high-pressure turbines (HPT) are directly exposed to combustion gases and to impingement of airborne particles,¹⁰ and consequently, corrosive attack is severe. This research is focusing on the validation of phase relationships and reaction sequences found on the pressure surface and the leading edge of an in-service EB-PVD YSZ coated first stage HPT blade. The present work benchmarks the corrosive effects of a multi-phase, essentially crystalline particle deposit with incongruent melting characteristics. Phase relationships are corroborated by powder syntheses and annealing experiments.

II. Experimental Procedure

The first stage HPT blade was provided by Lufthansa Technik AG, Power Plant Services-Engine Parts Repair (Hamburg, Germany). The accumulated in-service time was 17 000 h which is equivalent to approximately 3000 cycles of the engine in different operating regions. Similar HPT blades are employed for example in Pratt & Whitney 4000-type aero-engines. The HPT blade comprises a γ/γ' PWA 1484 Ni-base alloy, a two-phase $\gamma\text{-Ni}/\beta\text{-NiAl}$ low pressure plasma sprayed MCrAlY bond coat with Hf, Y, and Si added and a 7 wt% (4 mol%) EB-PVD YSZ top coat.¹¹

The microstructure of the blade's TBC system was surveyed in a scanning electron microscope (SEM) (Ultra 55; Carl Zeiss NTS, Wetzlar, Germany) equipped with an Inca energy-dispersive spectroscopy (EDS) system (Oxford Instruments, Abingdon, UK). Cross-section specimens from selected reactive interfaces were prepared for analytical transmission electron microscopy (TEM) via focused-ion-beam (FIB) sectioning through the lift-out technique, employing a single source FIB (Strata 205; FEI Inc., Eindhoven, The Netherlands). A 300 kV Tecnai F30 transmission electron microscope (FEI Inc.) with a field emission gun was utilized for analysis of FIB lamellae. Besides conventional TEM work, dark-field imaging in scanning transmission (STEM) mode employing a high-angle annular dark field (HAADF) detector was used for Z-contrast imaging in conjunction with energy-dispersive nanospectroscopy (EDS), selected area diffraction (SAD), and convergent-beam electron diffraction (CBED) for nanosized particles.

Starting materials for powder syntheses include Al (NO_3)₃·9H₂O, Ca(NO_3)₂·4H₂O, Mg(NO_3)₂·6H₂O, Fe(NO_3)₃·9H₂O, ZrO(NO_3)₂·xH₂O, (NH₄)₂SO₄, nanosized SiO₂, and TiO₂ (Merck, Darmstadt, Germany). A 4 mol% Y_2O_3 -stabilized ZrO_2 (TZ-4Y; Tosoh Chemicals, Tokyo, Japan) was used as reference powder. X-ray diffraction (XRD) phase analyses were performed in a D 5000 diffractometer utilizing $\text{CuK}\alpha$ radiation with secondary graphite monochromator (Bruker Analytical X-Ray Systems, Karlsruhe, Germany).

D. J. Green—contributing editor

Manuscript No. 29492. Received April 06, 2011; approved June 15, 2011.

[†]Author to whom correspondence should be addressed. e-mail: peter.mechnich@dlr.de.

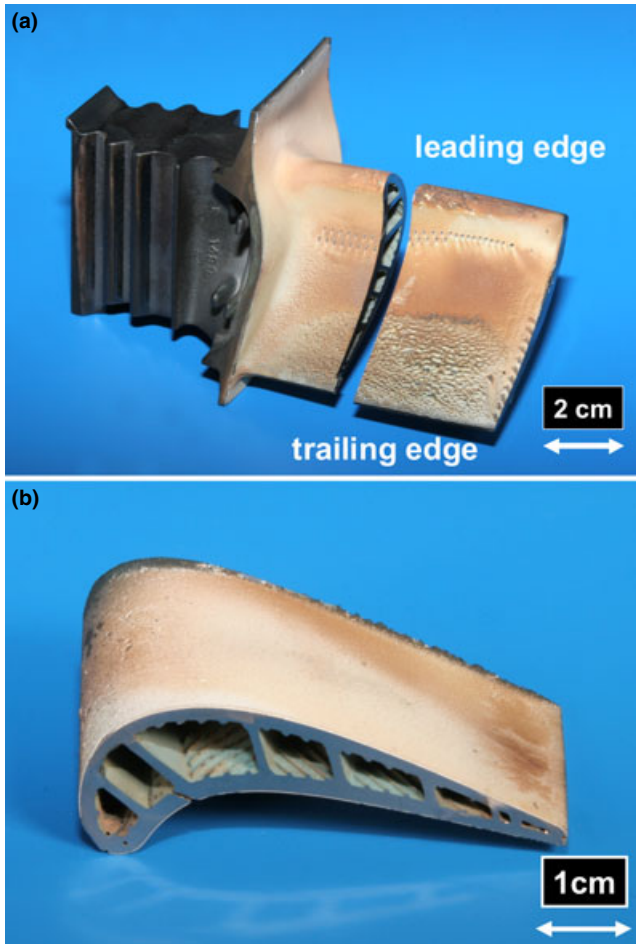


Fig. 1. The in-service HPT blade investigated (SE images). (a) Rough pressure surface holding numerous deposits at the trailing and fewer at the leading edge. (b) Smooth suction surface segment devoid of macroscopic deposits.

III. Results

(1) Microstructural Analysis of the In-Service HPT Blade

In general, the investigated turbine blade does not show critically damaged TBC areas. As depicted in Fig. 1(a) surface roughness of the pressure surface of the blade is high close to the trailing edge. Particle deposits are most abundant in this area and on the leading edge as well. The suction surface is tarnished [Fig. 1(b)], but appears macroscopically smoother holding, with few deposits only.

In this particular turbine blade CaSO_4 is a primary constituent at both, the pressure, and the suction surfaces as well as the leading edge. CaSO_4 infiltrates the intercolumnar pores of the coating and most of the thin feather arms through the full coating thickness (Fig. 2, thin section at the leading edge). Figure 3(a) displays a STEM dark field image from the YSZ/TGO interface. Figure 3(b) shows a $[1\ 0\ \bar{3}]$ zone axis pattern collected from the larger CaSO_4 pocket in Fig. 3(a), emphasizing that CaSO_4 is a fully crystalline anhydrite. Indexing of the electron diffraction pattern is based on the cell parameters given in Ref. ⁽¹²⁾. Small probe microanalysis (EDS) shows that anhydrite composition is stoichiometric with neither dissolved impurities nor Y or Zr from the coating. The overall anhydrite growth morphology is characterized by intergrowth of nanoscale columns to form distinct layers and platelet-type structures which have nucleated at free surfaces inside the pore channels (Fig. 4)

Figure 5 shows a SEM image of the top coat at the pressure surface close to the blade's trailing edge. The particle deposit appears granular and exhibits a patchy porosity. The average chemical bulk composition of the deposit was

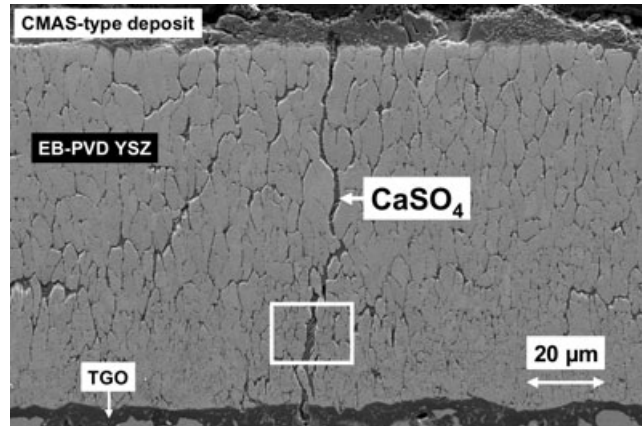


Fig. 2. Completely CaSO_4 -infiltrated EB-PVD YSZ top coat (SE image, trailing edge). Inset is shown in Fig. 4 at higher magnification.

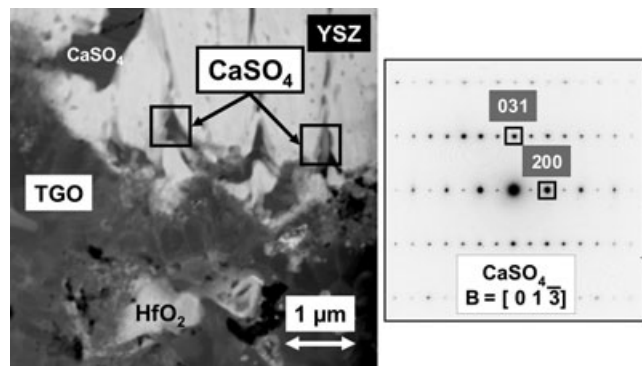


Fig. 3. (a) Anhydrite CaSO_4 pore fillings from lower coating section adjacent to the TGO layer (STEM HAADF image, leading edge). (b) SAD pattern taken from larger CaSO_4 pocket in (a).

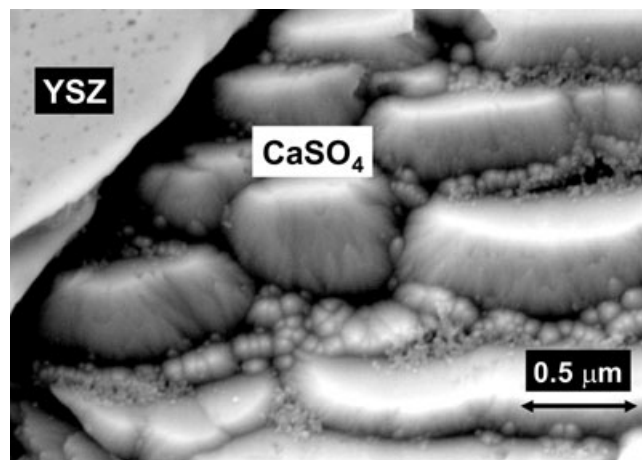


Fig. 4. Freestanding (unpolished) CaSO_4 microcrystals from marked location in Fig. 2 characterized by nanoscale columnar growth.

derived via EDS area microanalysis and is compared in Table I with frequently referred CMAS literature data.⁹ The Al_2O_3 concentration in the present deposit is about the same and the MgO concentration is higher. In contrast to the model CMAS, the present deposit contains significant amounts of Fe_2O_3 and TiO_2 . To recognize this fact, the deposit composition is now referred to as Fe-Ti-CMAS (“FTCMAS”). Between the CaSO_4 -filled YSZ columns and the FTCMAS deposit, a pronounced reactive interface with

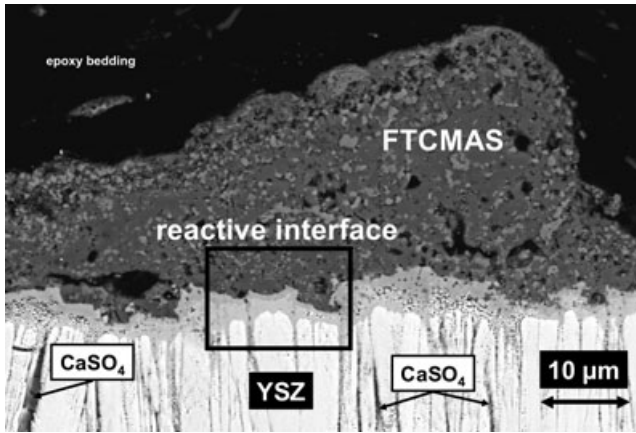


Fig. 5. FTCMAS deposited on YSZ top coat fully infiltrated with CaSO_4 (SE image, pressure surface close to trailing edge). Boxed region is displayed at higher magnification in Fig. 6.

Table I. Chemical Compositions of CMAS-Type Materials

[mol%]	Model CMAS ⁹	Deposit on HPT-Airfoil (this work)	Model Fe,Ti-CMAS (this work)
CaO	35.3	39.3	41.0
MgO	9.6	16.1	16.8
Al_2O_3	6.9	6.5	6.8
SiO_2	48.2	24.4	25.5
TiO_2		2.5	2.6
Fe_2O_3		7.0	7.3
NiO		0.7	
SO_3		2.6	
P_2O_5		0.4	
ZrO_2		0.5	

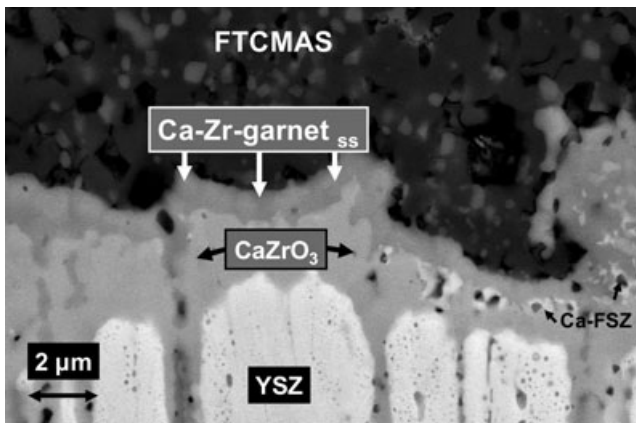


Fig. 6. FTCMAS/YSZ reactive interface (close-up from boxed region in Fig. 5) including garnet (kimzeyite) layer followed by CaZrO_3 -layer with some dispersed Ca-FSZ particles. Note blunting of YSZ column tips (BSE image).

an average thickness of approximately $5 \mu\text{m}$ is clearly visible. Figure 6 depicts a close-up of the marked area in Fig. 5. Blunted YSZ column tips are covered by a continuous CaZrO_3 layer. On the right hand part of the image, the CaZrO_3 layer additionally exhibits dispersed Ca-stabilized, cubic ZrO_2 grains (fully stabilized ZrO_2 , FSZ). The CaO concentration of the Ca-FSZ grains was of the order of 12 wt%, some grains were co-stabilized with an additional 1.5 wt% Y_2O_3 . Between the CaZrO_3 layer and the FTCMAS, a second newly formed phase is stabilized. EDS analysis reveals

that this phase contains considerable amounts of ZrO_2 , CaO , Fe_2O_3 , TiO_2 , SiO_2 , and Al_2O_3 .

A detailed examination of the phase relationships at the reactive interface was achieved through a combination of electron diffraction and EDS microanalysis. A STEM dark field image of a reactive interface is displayed in Fig. 7(a). The blunted YSZ column tips are covered by the continuous CaZrO_3 layer. A SAD pattern of CaZrO_3 oriented parallel to [012] is shown in Fig. 7(c), with indexing according to ICDD PDF-file no. 35-0790. Only Fe traces are detected in CaZrO_3 , while small amounts of Fe, Ti, and Ca are found close to YSZ columns. The marked change from the faceted YSZ tip morphology in the as-coated condition to blunted tip morphology in the corroded state obviously is due to partial zirconia dissolution. The YSZ tips were co-stabilized by CaO and Y_2O_3 which changed for the standard YSZ composition when analyzed further away from the interface. The phase in between CaZrO_3 and the FTCMAS deposit is unambiguously identified as the mineral kimzeyite with the empirical formula $\text{Ca}_3(\text{Zr,Ti,Fe})_2(\text{Al,Fe,Si})_3\text{O}_{12}$ [ICDD PDF-file no. 13-0130]. Small garnet microcrystals from the reactive interface are conveniently investigated in CBED mode, a [011] zone axis composite diffraction pattern with the zero Laue zone (ZOLZ) pattern superimposed on the first- and second order Laue (FOLZ, SOLZ) zone ring structure is displayed in Fig. 7(b). Note the anhydrite phase sealing the pore channel just below the CaZrO_3 /kimzeyite layer.

Despite minor morphological differences the major locations of the turbine blade share the same phase assemblage at the FTCMAS/YSZ interface. Figure 8 shows an example of an FTCMAS/YSZ reaction zone from the leading edge. In this case, CaZrO_3 and kimzeyite-type garnet form an interpenetrating interface without dispersion of Ca-FSZ particles.

(2) Examination of Phase Equilibria by Annealing of Synthetic Powder Mixtures

The complex microstructure of the in-service TBC raises the question whether or not the microscopically observed phase relationships can be accessed in a simplified laboratory approach. Basically, three major reactive interfaces can be distinguished in the TBC:

1. Anhydrite is found as through-thickness inter- and intra-columnar pore filling of EB-PVD YSZ TBC.
2. A zone consisting of CaZrO_3 and cubic FSZ exists close to the YSZ columns tips.
3. A kimzeyite layer separates the CaZrO_3 /FSZ zone from the FTCMAS deposit.

It is anticipated that this sequence reflects the availability of reactive species as well as the temperature gradient across the TBC system during service. To examine these phase relationships, annealing experiments using powder mixtures were carried out.

(A) *The $\text{CaSO}_4/4 \text{ mol}\% \text{ Y}_2\text{O}_3$ -Stabilized ZrO_2 Reaction Couple:* A single-phase anhydrite powder (CaSO_4) was prepared by co-precipitation of aqueous solutions of $\text{Ca}(\text{NO}_3)_2 \cdot 4\text{H}_2\text{O}$ and $(\text{NH}_4)_2\text{SO}_4$ followed by annealing of the precipitates at 1000°C . To study the phase stability, a 50/50 wt% powder mixture of CaSO_4 and tetragonal 4 mol% YSZ (t-YSZ) was annealed at 1100°C , 1150°C and 1200°C for 1 h, respectively. The results of the XRD analyses are given in Fig. 9. After annealing at 1100°C , the powder mixture still consists of the starting materials CaSO_4 and t-YSZ. After annealing at 1150°C , additional XRD reflections appear e.g., at approximately 22° , 45° , and $57^\circ 2\theta$, respectively. The same effect is observed to a much larger extent upon annealing at 1200°C . The newly formed phase is identified unambiguously as being CaZrO_3 . A second, significant effect is observed for t-YSZ. The tetragonal crystal structure is still

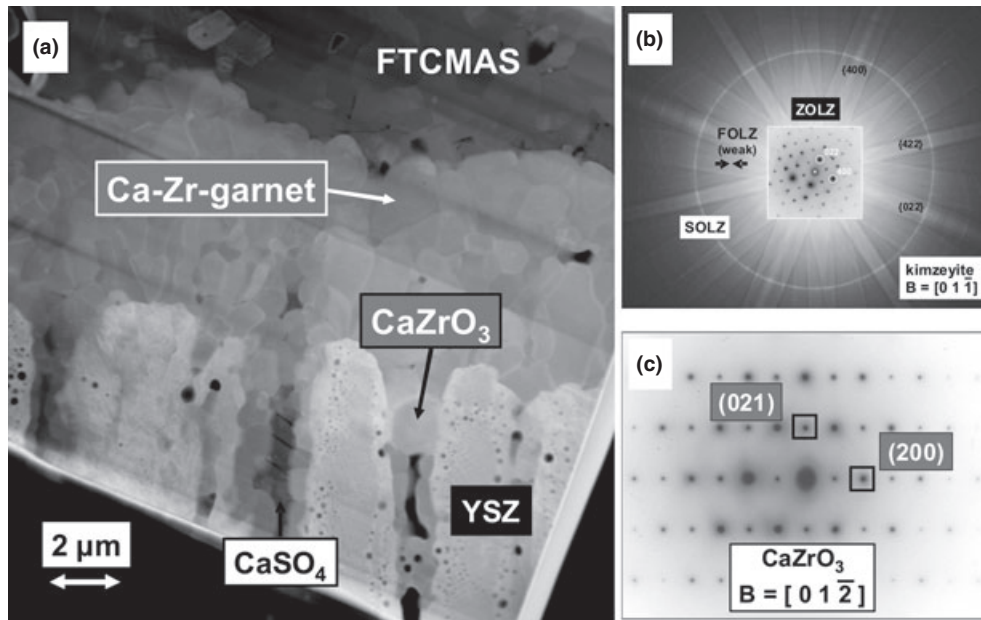


Fig. 7. Validation of CaZrO_3 and Ca-Zr-garnet (kimzeyite) from the reactive FTCMAS/YSZ interface via electron diffraction. (a) Low magnification overview of garnet/ CaZrO_3 reaction layer (STEM, HAADF). Diffraction patterns in (b) and (c) collected from positions indicated. (b) composite SAD/CBED pattern of garnet phase including the zero order Laue zone (ZOLZ) and the rings of the first and second order Laue zone (FOLZ, SOLZ), respectively. (c) CaZrO_3 SAD pattern.

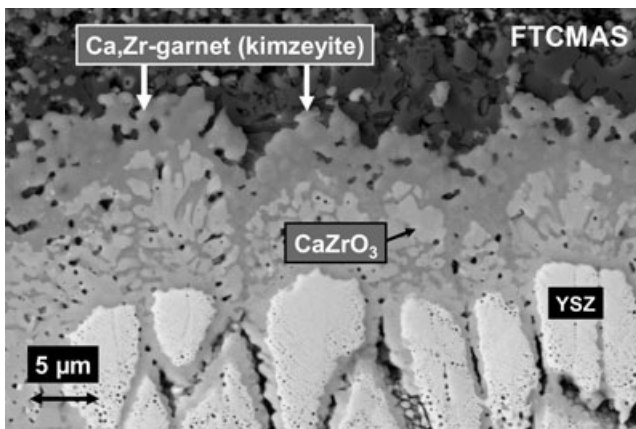


Fig. 8. FTCMAS/YSZ reaction zone from the leading edge displaying the CaZrO_3 /kimzeyite double layer (BSE image).

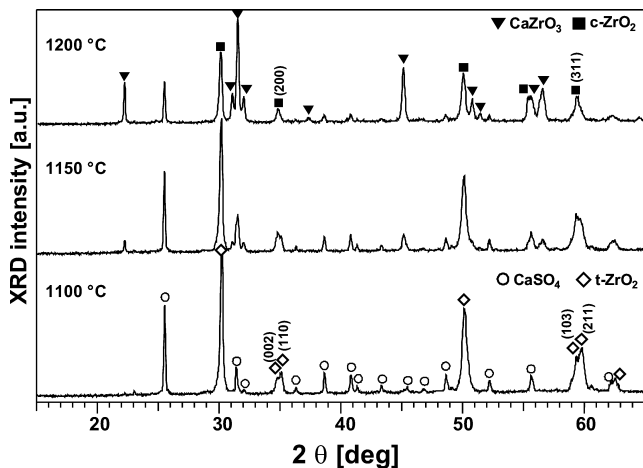


Fig. 9. XRD profiles of a 50:50 wt% $\text{CaSO}_4/4$ mol% Y_2O_3 stabilized ZrO_2 reaction pair upon a 1 h annealing at 1100°C, 1150°C, and 1200°C indicating a threshold temperature of 1150°C for CaZrO_3 formation. Symbols include CaSO_4 (open circles), t- ZrO_2 (open diamonds), c- ZrO_2 (full squares), and CaZrO_3 (full triangles).

valid at 1100°C as indicated by successful indexing in the crystallographic space-group $P4_2/nmc$ (no. 137). As representative examples the XRD-reflection pairs (002)/(110) and (103)/(211) are highlighted in Fig. 9. However, at 1150°C there is a significant change of position, shape, and intensity of these XRD peaks. After annealing at 1200°C, a discrimination of the tetragonal (002)/(110) and (103)/(211) reflections is not possible, instead the reflections can be indexed as (200) and (311) in the cubic space group $Fm\bar{3}m$. Therefore, fully stabilized, cubic ZrO_2 is now the prevalent YSZ polymorph. Two mechanisms may be derived from this effect. First, the formation of CaZrO_3 at the expense of ZrO_2 may lead to an enrichment of stabilizing Y_2O_3 in the residual YSZ. Second, excess Ca not consumed during the formation of CaZrO_3 may diffuse into YSZ providing stabilization of the cubic phase. From the annealing experiments it can be concluded that the onset temperature for the formation of CaZrO_3 and fully stabilized, cubic ZrO_2 at the expense of t- ZrO_2 and CaSO_4 is approximately 1150°C.

(B) The CaZrO_3 /FTCMAS Reaction Couple: To access the FTCMAS-deposit retrieved from the turbine blade, an FTCMAS powder was synthesized by thermal decomposition of metal nitrates along with nanosized SiO_2 and TiO_2 . For this purpose the original blade FTCMAS composition was normalized to the Fe_2O_3 - TiO_2 - CaO - MgO - Al_2O_3 - SiO_2 -system (Table I). Upon annealing for 1 h at 1250°C, synthetic FTCMAS consists of a melilite-type phase, a spinel-type ferrite, merwinite, and a perovskite-type calcium-titanate (XRD analysis in Fig. 10). Melilite refers to tetragonal solid solutions between the end members gehlenite ($\text{Ca}_3\text{Al}_2\text{SiO}_7$) and akermanite ($\text{Ca}_2\text{MgSi}_2\text{O}_7$). The SEM image [Fig. 11(a)] shows a polished cross section of synthetic FTCMAS after annealing at 1250°C. All phases exhibit characteristic microstructural features. Melilite forms the dominant phase exhibiting only weak grain orientation contrasts. Quantitative EDX-analysis yields a molar chemical composition of 44% CaO, 10% MgO, 10% Al_2O_3 , 33% SiO_2 , and 3% Fe_2O_3 . Assuming Fe_2O_3 substituting Al_2O_3 in the gehlenite component, the present melilite can be assigned to a nearly 1:1 solid solution of gehlenite and akermanite. Spinel-type ferrite $\text{Mg}(\text{Al},\text{Fe})_2\text{O}_4$ forms high-relief prismatic grains. Quantitative EDX-analysis of this phase confirms an

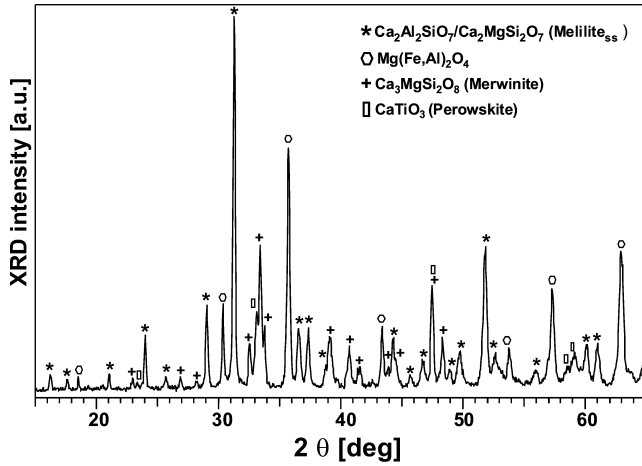


Fig. 10. XRD profile of synthetic FTCMAS batch upon annealing at 1250°C/1 h revealing a four-phase assemblage including gehlenite-rich melilite solid solution (ss) $\text{Ca}_2(\text{Mg,Al})(\text{Si,Al})\text{SiO}_7$ (stars), Fe-rich spinel ss $\text{Mg}(\text{Fe,Al})_2\text{O}_4$ (open hexagons), merwinite $\text{Ca}_3\text{MgSi}_2\text{O}_8$ (crosses), and perovskite CaTiO_3 (rectangles), respectively.

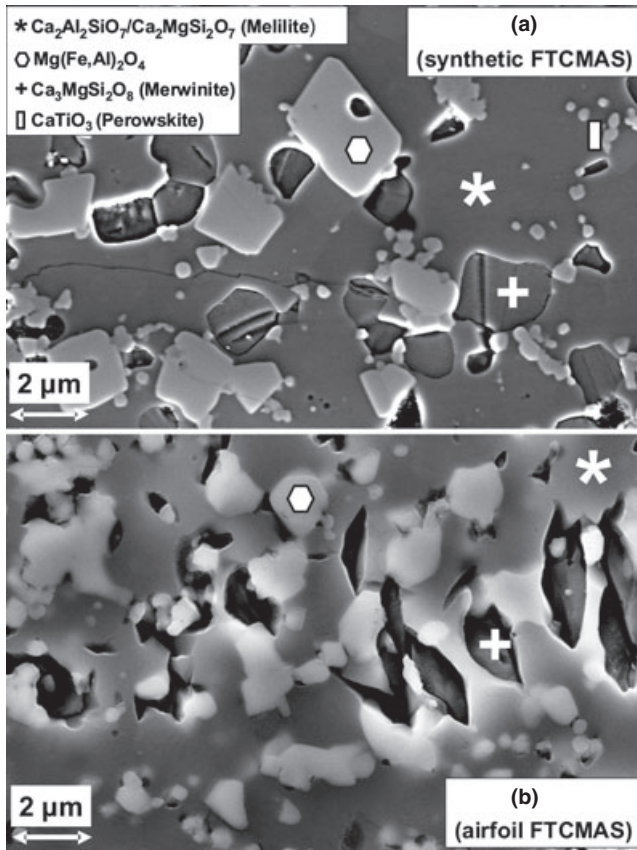


Fig. 11. Matching (a) synthetic FTCMAS and (b) real FTCMAS deposit from HPT blade (pressure surface) (SE images). Phase assemblages consist of melilite solid solution (ss), $\text{Ca}_2(\text{Mg,Al})(\text{Si,Al})\text{SiO}_7$ (stars), spinel ss $\text{Mg}(\text{Fe,Al})_2\text{O}_4$ (hexagons) along with merwinite $\text{Ca}_3\text{MgSi}_2\text{O}_8$ (crosses). CaTiO_3 is identified only in synthetic sample (a).

iron-rich solid solution $\text{Mg}(\text{Fe}_{0.83}\text{Al}_{0.17})_2\text{O}_4$. Merwinite $\text{Ca}_3\text{MgSi}_2\text{O}_8$ grains typically exhibit a low relief along with a textured surface. Perovskite-type CaTiO_3 crystals are small and form isolated clusters. EDS analyses reveal that both merwinite and perovskite crystals are essentially stoichiometric. SEM images confirm the very good agreement between the synthetic FTCMAS and the genuine FTCMAS retrieved from the turbine blade [Fig. 11(b)].

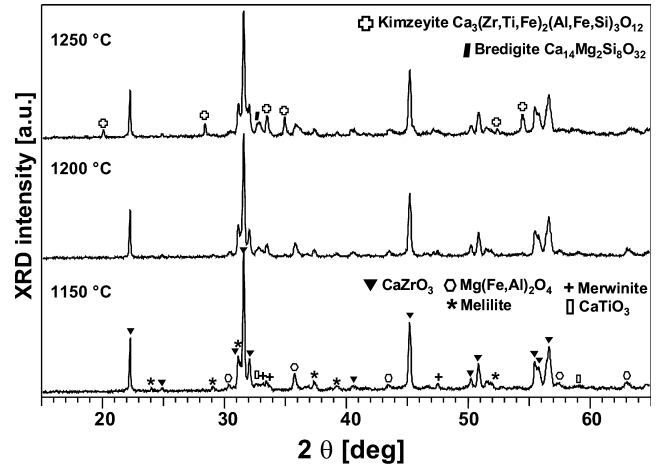


Fig. 12. XRD profile of a 50:50 wt% CaZrO_3 /FTCMAS powder mixture upon an 1 h annealing at 1150°C, 1200°C, and 1250°C, respectively, revealing a substantial amount of newly formed kimzeyite at 1250°C. Due to excess CaZrO_3 in the starting mixture CaZrO_3 still prevails upon kimzeyite formation. Symbols include kimzeyite (open squares), CaZrO_3 (full triangles), $\text{Mg}(\text{Fe,Al})_2\text{O}_4$ spinel (open hexagons), melilite (stars), merwinite (crosses), perovskite CaTiO_3 (rectangles), and bredigite $\text{Ca}_{14}\text{Mg}_2\text{Si}_8\text{O}_{32}$ (full rhomboids).

A single phase CaZrO_3 powder was prepared by co-decomposition of $\text{Ca}(\text{NO}_3)_2 \cdot 4\text{H}_2\text{O}$ and $\text{ZrO}(\text{NO}_3)_2 \cdot x\text{H}_2\text{O}$ followed by annealing at 1200°C. Consistent with the CaSO_4 /t-YSZ annealing experiments, a 50/50 wt% powder mixture of CaZrO_3 and synthetic FTCMAS was annealed. Figure 12 shows the XRD analyses after 1 h annealing at 1150°C, 1200°C and 1250°C, respectively. After the annealing at 1150°C, the powder mixture still consists of the starting materials, i.e., CaZrO_3 and the crystalline FTCMAS phases. At 1200°C there seems to be no significant reaction between CaZrO_3 and FTCMAS at first glance. However, the XRD peak intensities of both merwinite and melilite reflections decrease. After annealing at 1250°C new XRD peaks appear, unambiguously belonging to the kimzeyite-type garnet phase. A broad, probably multiple XRD reflection at approximately $33^\circ 2\theta$ may be associated with the orthorhombic phase bredigite $\text{Ca}_{14}\text{Mg}_2\text{Si}_8\text{O}_{32}$. From these annealing experiments it is concluded that kimzeyite forms at the expense of CaZrO_3 and FTCMAS as soon as the temperatures exceed 1200°C.

IV. Discussion

The YSZ TBC of the investigated in-service turbine blade exhibits a characteristic corrosion scenario representing a cumulative response to the specific engine operation range. In the present case a CaSO_4 pore filling and a FTCMAS-type particle deposit are the two dominating impurity sources. Along with these reactive species, a characteristic in-service temperature gradient across the YSZ top coat is evident. Anhydrite growth morphology is characterized by intergrowth of nanoscale columns extending into a platelet-type morphology (Fig. 4). The complete filling of even very small pores, the grain morphology and the remarkable high chemical purity cannot reasonably be explained with CaSO_4 crystallized from a liquid phase. On the other hand, the striking microstructural similarities with anhydrite built via magmatic vapor condensation during volcanic eruptions¹³ suggest that anhydrite deposition on the YSZ pore walls from a Ca- and S-rich gas phase may be a likely formation mechanism during turbine operation. The thermal compatibility of CaSO_4 and YSZ, however, was found to be limited to temperatures in the 1100°C range. Above 1100°C the stabilization of CaZrO_3 and a co-existing FSZ phase was observed in lab-scale annealing experiments. The microstructural features from the blade's reactive interfaces support the idea that at temperatures above the 1100°C threshold a CaZrO_3 /FSZ layer is

formed at the expense of the YSZ column tips and CaSO_4 . At lower temperatures CaSO_4 pore filling and YSZ pore walls co-exist.

The second major source contributing to TBC recession is related to the airborne mineral particles ingested by the turbine and accumulated on the YSZ surface. It should be kept in mind that deposit bulk-compositions are case-specific, reflecting the engine operation range. In contrast to the four-component CMAS model systems the present FTCMAS deposits are crystalline and exhibit a much lower SiO_2 content. The substantial Fe_2O_3 and TiO_2 concentrations in these CMAS-type deposits emphasize the need to introduce an expanded "FTCMAS" system (Table I). This extended chemical composition is plausible since both Fe_2O_3 and TiO_2 are main constituents of the lithosphere, i.e., of rock-forming minerals which are a major source of airborne inorganic particles. Whereas the congruent-type melting model CMAS gives rise to ZrO_2 solution/precipitation in the root section of the melt-infiltrated top coat,⁹ chemical reactions between YSZ surface and the crystalline FTCMAS particle deposit occur predominantly in solid state.

From the FTCMAS composition rather complex phase relationships may be expected at the FTCMAS/ CaZrO_3 reactive interface. Instead, a single phase layer of kimzeyite is formed. Kimzeyite, the only natural Ca-garnet containing Zr as a major constituent, is a rare accessory mineral from carbonatite rocks¹⁴ and has triggered interest as a potential nuclear waste storage material.¹⁵ Although ternary Ca-Zr-silicates may also occur in specific regions of turbine blades,^{11,16} it was not before this work that the significance of the garnet phase has been fully recognized in the context of turbine airfoil recession. Owing to its crystal chemistry, kimzeyite represents an almost ideal sink at the FTCMAS/YSZ interface. In the general garnet structure $\text{X}_3^{[8]}\text{Y}_2^{[6]}\text{Z}_3^{[4]}\text{O}_{12}$ the ZO_4 tetrahedra ($\text{Z} = \text{Al}^{3+}, \text{Fe}^{3+}, \text{Si}^{4+}$) are linked by Y-cation octahedra ($\text{Y} = \text{Zr}^{2+}, \text{Y}^{3+}, \text{Ti}^{4+}, \text{Fe}^{2+}$), while the larger divalent X-cations ($\text{X} = \text{Ca}^{2+}, \text{Mg}^{2+}$) are located on the dodecahedral X-site in the center of the island silicate framework. As expressed by the so-called kimzeyite-type substitution mechanism¹⁷ $\text{Zr}^{4+}(\text{Y}) + \text{Me}^{3+}(\text{Z}) \leftrightarrow \text{Si}^{4+}(\text{Z}) + \text{Me}^{3+}(\text{Y})$ ($\text{Me}^{3+} = \text{Al}, \text{Fe}$), a high Zr^{4+} -level garnet requires cation distribution over the octahedrally coordinated Y-site and the tetrahedral Z-site. A similar cation substitution mechanism involves the Ti^{4+} sites. Therefore kimzeyite-type garnets can comfortably accommodate chemical gradients across the FTCMAS/YSZ interface. The molar chemical bulk composition of kimzeyite was determined using EDS microanalysis to be approximately 40% CaO , 18% ZrO_2 , 16% SiO_2 , 10% Fe_2O_3 , 9% TiO_3 , 4% Al_2O_3 , and 2% MgO . Y_2O_3 is detected, but the concentration is too low for accurate EDS quantification. The re-calculation of the kimzeyite mineral formula (based on 12 oxygen atoms per formula unit) yields $(\text{Ca}_{0.95}\text{Mg}_{0.05})_3(\text{Zr}_{0.67}\text{Ti}_{0.33})_2(\text{Al}_{0.18}\text{Fe}_{0.45}\text{Si}_{0.37})_3\text{O}_{12}$. Following ref. (15), Fe is positioned solely as Fe^{3+} on the Z-site. In addition to Zr and Mg, trace Y will most likely also enter the X-position.

The blade results clearly indicate that the preferred formation of kimzeyite over CaZrO_3 is controlled by the abundance of Fe, Ti, and Si at the interface. Due to the limited homogeneity range of the perovskite-type structure a single CaZrO_3 layer is solely found at pure CaSO_4 /YSZ interfaces. A supplementary series of annealing experiments was conducted to highlight the interplay of FTCMAS with CaZrO_3 producing the notable CaZrO_3 /kimzeyite double layer which is observed at most turbine blade surfaces holding FTCMAS particles. The key argument for rationalizing this double layer is related to the fact that even for Ca- and Zr-rich environments CaZrO_3 is stable under zero or very low Si-activity conditions only.¹⁸ We have shown that CaZrO_3 easily forms at the expense of CaSO_4 and YSZ (Fig. 8) above 1100°C. The Ca gradient at the reactive interface then gives rise to the observed sequence $\text{CaZrO}_3 \rightarrow \text{Ca/Y-FSZ} \rightarrow \text{YSZ}$, as

expected from phase relationships in the ternary $\text{CaO}-\text{Y}_2\text{O}_3-\text{ZrO}_2$.^{16,19} On the other hand, substantial kimzeyite-type garnet was formed upon annealing of a FTCMAS/ CaZrO_3 powder mixture at 1250°C. This confirms the thermodynamic instability of CaZrO_3 as soon as the corrosion environment becomes Fe-, Ti, and Si-bearing. The microstructure of the blade's reactive interface as well as phase compatibilities derived from the supplementary annealing experiments support the idea of a dual corrosion process:

1. A first stage controlled by a Si-free Ca-source, most likely primary gas-phase derived CaSO_4 producing a thin CaZrO_3 layer on the top coat
2. A second stage with high Fe, Ti, and Si-activity unfavorable for CaZrO_3 thus stabilizing kimzeyite instead.

It is anticipated that both corrosion mechanisms are cumulative and may also proceed simultaneously. Under the present HPT operation conditions, the FTCMAS deposit did not provide substantial melt phase which is able to seal the YSZ TBC. Hence even an extensive FTCMAS particle coverage of the turbine blade will not prevent gas-phase condensation of CaSO_4 in YSZ pore channels. However, since the investigation did not reveal YSZ/kimzeyite interfaces (i.e., without CaZrO_3 interlayer), there is evidence that the Si-free corrosion stage favoring CaZrO_3 formation is primary.

In terms of the different threshold temperatures derived for CaZrO_3 and kimzeyite formation from our short-term sintering experiments, a turbine blade surface temperature in the 1200°C range appears reasonable (Fig. 13) and is in agreement with modeled surface temperatures of TBC-coated turbine blades.²⁰ Thus, the presence of a CaZrO_3 /kimzeyite double layer may be used as a gauge for estimating effective in-service temperatures at the turbine blade's YSZ TBC.

With respect to long-term TBC integrity, both corrosion mechanisms exhibit beneficial features which may compensate the disadvantageous destabilization of YSZ. At the hot coating surface, the thin CaZrO_3 /kimzeyite double layer provides an effective diffusion barrier for CMAS constituents. Further mitigation of reactive species may be provided by CaSO_4 filling of the bulk coating porosity. The low mismatch stresses introduced by similar coefficients of thermal expansion of 7-YSZ ($\alpha \sim 11$ ppm/K)²¹ and CaSO_4 ($\alpha \sim 11$ ppm/K)²² are seemingly favorable for long-term thermocyclic operation.²³ On the other hand, TBC strain tolerance will presumably be deteriorated by the thin CaZrO_3 /kimzeyite surface layer and, in particular, the CaSO_4 filling of bulk

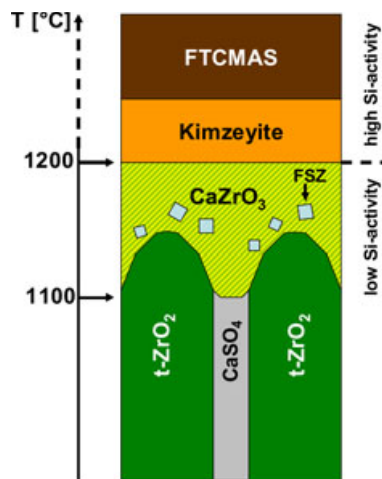


Fig. 13. Schematic of the reactive interfaces from HPT blade with fully infiltrated YSZ TBC in the light of the (i) experimentally derived formation temperatures for the interfacial compounds CaZrO_3 and garnet phase (kimzeyite) and (ii) essential environmental constraints (low vs. high Si-activity) during hot-corrosion. Note that CaSO_4 may deposit simultaneously to FTCMAS particles once the top coat infiltration by CaSO_4 is completed.

YSZ intercolumnar porosity. It is difficult to rate these effects from post-service fractographic analysis where also preparation-induced artifacts are not unlikely. Nonetheless, the investigated airfoil emphasizes the moderate impact of the CaSO₄-infiltration on the overall structural integrity of the EB-PVDYSZ TBC. Owing to its wide homogeneity range, the kimzeyite-type garnet structure provides an effective sink for FTCMAS constituents thus leveling the chemical gradient and consequently reducing the driving force for YSZ dissolution. If turbine blade surface peak temperatures are kept below the melting temperature of kimzeyite (approximately 1290°C),²⁴ a stable operation of the TBC system is possible for even prolonged operating times. It should, however, be kept in mind that our laboratory experiments were performed in ambient atmosphere. Important parameters effecting reaction kinetics, such as the significant water partial pressure of the combustion gas, may shift the stability limit of kimzeyite-type garnets toward considerable lower temperatures. In the light of future engines designed for much higher turbine inlet temperatures, the formation and melting behavior of kimzeyite is considered to be one of the key limiting factors of ZrO₂-based TBC materials. Further work is in progress to address these open issues.

V. Conclusions

In-service recession of an EB-PVD YSZ coated first stage HPT blade is exploited via analytical electron microscopy and concomitant laboratory annealing experiments. Complete CaSO₄ infiltration of the YSZ TBC along with deposition of airborne mineral particles adds to the complexity of the system.

Unlike CMAS compositions from the literature, small probe microanalysis of the turbine blade's particle deposits reveals a high CaO/SiO₂ ratio and considerable Fe₂O₃ and TiO₂ concentrations. This observation is the reason for introducing an expanded Fe-Ti-CMAS "FTCMAS" system. Upon solid state reaction of YSZ with CaSO₄ and/or the FTCMAS deposits distinct reactive interfaces are observed. Major constituents are CaZrO₃ enveloping blunted YSZ tips and the kimzeyite-type garnet phase (Ca,Mg)₃(Zr,Ti,Fe)₂(Al,Fe,Si)₃O₁₂ separating CaZrO₃ from the FTCMAS deposit. The prevalent CaZrO₃/kimzeyite double layer is identified as an indicator for a dual corrosion process effective during turbine blade operation with CaZrO₃ built from a Si-free Ca-source, most likely gas-phase derived CaSO₄, and a high Si-activity, Fe₂O₃ and TiO₂ rich FTCMAS deposit stabilizing kimzeyite instead. Kimzeyite exhibits a large solid solution range thus balancing the chemical gradient at the reactive interface. Long-term mitigation of reactive species is provided by CaSO₄ filling of the coating porosity. A stabilization of the reactive interfaces is anticipated for even prolonged operating times if peak surface temperatures of the turbine blade remain below the melting point of kimzeyite.

Acknowledgments

We thank C. W. Siry, O. Schubert and T. Fischer of Lufthansa Technik AG, Power Plant Services-Engine Parts Repair, Hamburg, Germany for providing the turbine blade.

References

- N. P. Padture, M. Gell, and E. H. Jordan, "Thermal Barrier Coatings for Gas-Turbine Engine Applications," *Science*, **296**, 280-4 (2002).
- J.L. Smialek, F.A. Archer, and R.G. Garlick, "The Chemistry of Saudi Arabian Sand: A Deposition Problem on Helicopter Turbine Airfoils"; pp. M63-M77 in *Advances in Synthesis and Processes*, Edited by F.H. Froes. 3rd Int. SAMPE Metals Conference, 1992
- F.H. Stott, D.J. de Wet, and R. Taylor, "The Effect of Molten Silicate Deposits on the Stability of Thermal Barrier Coatings for Turbine Applications at Very High Temperatures"; pp. M92-M101 in *Advances in Synthesis and Processes*, Edited by F.H. Froes. 3rd Int. SAMPE Metals Conference, 1992
- D. J. de Wet, R. Taylor, and F. H. Stott, "Corrosion Mechanisms of ZrO₂-Y₂O₃ Thermal Barrier Coatings in the Presence of Molten Middle-East Sand," *J. Phys. IV*, **3** [C9] 655-63 (1993).
- F. H. Stott, D. J. de Wet, and R. Taylor, "Degradation of Thermal Barrier Coatings at Very High Temperatures," *MRS Bull.*, **19** [10] 46-9 (1994).
- J. L. Smialek, F. A. Archer, and R. G. Garlick, "Turbine Airfoil Degradation in the Persian Gulf War," *J. Min. Metall. Mater. Soc.*, **46** [12] 39-41 (1994).
- W. S. Walsh, K. A. Thole, and C. Joe, "Effects of Sand Ingestion on the Blockage of Film-Cooling Holes"; pp. 1-10 in *Proceedings of ASME Turbo Expo*, May 8-11, Barcelona, Spain, 2006, Paper GT2006-90067.
- M. P. Borom, C. A. Johnson, and L. A. Peluso, "Role of Environmental Deposits and Operating Surface Temperature in Spallation of Air Plasma Sprayed Thermal Barrier Coatings," *Surf. Coat. Technol.*, **86-87**, 116-26 (1996).
- S. Krämer, J. Yang, C. G. Levi, and C. A. J. Johnson, "Thermochemical Interaction of Thermal Barrier Coatings with Molten CaO-MgO-Al₂O₃-SiO₂ (CMAS) Deposits," *J. Am. Ceram. Soc.*, **89** [10] 3167-75 (2006).
- C. W. Siry, H. Wanzek, and C. P. Dau, "Aspects of TBC Service Experience in Aero Engines," *Mat.-Wiss. u. Werkstofftechnik*, **32**, 650-3 (2001).
- W. Braue, "Environmental Stability of the YSZ Layer and the YSZ/TGO Interface of an In-Service EB-PVD Coated High-Pressure Turbine Blade," *J. Mater. Sci.*, **44**, 1664-75 (2009).
- A. Kirfel and G. Will, "Charge Density of Anhydrite, CaSO₄, from X-ray and Neutron Diffraction Measurements," *Acta Cryst. B*, **36**, 2881-90 (1980).
- R. T. Jakubowski, J. Fournelle, S. Welch, R. J. Swope, and P. Camus, "Evidence for Magmatic Vapor Deposition of Anhydrite Prior to the 1991 Climatic Eruption of Mount Pinatubo, Philippines," *Am. Mineral.*, **87**, 1029-45 (2002).
- C. Milton, B. L. Ingram, and L. V. Blade, "Kimzeyite, a Zirconium Garnet from Magnet Cove, Arkansas," *Am. Mineral.*, **46**, 533-48 (1961).
- K. R. Whittle, G. R. Lumpkin, F. J. Berry, G. Oates, K. L. Smith, S. Yudinsev, and N. J. Zalusec, "The Structure and Ordering of Zirconium and Hafnium Containing Garnets Studied by Electron Channeling, Neutron Diffraction and Mössbauer Spectroscopy," *J. Solid State Chem.*, **180**, 785-91 (2007).
- S. S. Pandit and K. T. Jacob, "Phase Relations in the System CaO-SiO₂-ZrO₂ at 1573 K," *Steel Res.*, **65**, 410-3 (1994).
- E. Schingaro, F. Scordari, F. Capitanio, G. Parodi, D. C. Smith, and A. Mottana, "Crystal Chemistry of Kimzeyite from Anguillara, Mts. Sabatani, Italy," *Eur. J. Mineral.*, **13**, 749-59 (2001).
- E. V. Galuskin, N. N. Pertsev, P. Dzierzanowski, M. Kadiyski, A. G. Gurbanov, R. Wrzalik, and A. Winiarski, "Lakargiite CaZrO₃: A New Mineral from the Perovskite Group from the North Caucasus, Kabardino-Balkaria, Russia," *Am. Mineral.*, **93**, 1903-10 (2008).
- H. M. Ondik and H. F. McMurdie, *Phase Diagrams for Zirconium and Zirconia Systems*. The American Ceramic Society, Westerville, OH, 1998.
- R. A. Miller, "Thermal Barrier Coatings for Aircraft Engines: History and Directions," *J. Therm. Spray Tech.*, **6**, 35-42 (1997).
- A. G. Evans, D. R. Mumm, J. W. Hutchison, G. H. Meier, and F. S. Petit, "Mechanisms Controlling the Durability of Thermal Barrier Coatings," *Prog. Mater. Sci.*, **46**, 505-53 (2001).
- A. A. Khan, "Computer Simulation of Thermal Expansion of Non-Cubic Crystals: Forsterite, Anhydrite, and Scheelite," *Acta Cryst. A*, **32**, 11-6 (1976).
- G. Witz, V. Shklover, W. Steurer, S. Bachegowda, and H. P. Bossmann, "High-Temperature Interaction of Ytria Stabilized Zirconia Coatings with CaO-MgO-Al₂O₃-SiO₂ (CMAS) Deposits," *Surf. Coat. Technol.* (2009), doi: 10.1016/j.surfcoat.2009.07.034 (in press)
- J. Ito and C. Frondel, "Synthetic Zirconium and Titanium Garnets," *Am. Mineral.*, **52**, 773-81 (1967). □